Civil Engineering Beyond Limits 2 (2026) 11112
Civil Engineering Beyond Limits
journal home: www.acapublishing.com/journals/1/cebel

Research Article

Comparative performance assessment of optical flow methods for vision-based structural identification using vibration data

Selenay Gençcelep[1], Volkan Kahya[*,2], Kemal Hacıefendioğlu[3]
[1,2,3]*Karadeniz Technical University, Faculty of Engineering, Department of Civil Engineering, 61080 Trabzon, Türkiye*

Keywords

*Optical flow,
Vibration measurement,
Vision-based identification,
Operational modal analysis,
Structural health monitoring.*

Abstract

This study presents a comparative performance assessment of four vision-based motion extraction approaches—Lucas–Kanade, Farnebäck, Horn–Schunck, and a phase-based method—for vibration identification and modal parameter estimation in a laboratory-scale single-story reinforced concrete (RC) frame subjected to controlled impact excitation. High-speed video recordings (216 fps) are processed through a custom-developed graphical user interface that standardizes region-of-interest (ROI) selection, pixel-to-length calibration, displacement extraction, and data export, enabling a fair algorithm-to-algorithm comparison under identical experimental conditions. Displacement time histories obtained from each method are evaluated in both the frequency domain using the Fast Fourier Transform (FFT) and in the modal domain via Operational Modal Analysis (OMA) implemented in the PyOMA_GUI environment. The comparison focuses on the low-amplitude vibration regime, where optical-flow robustness and noise sensitivity become critical. The results indicate that Lucas–Kanade and Farnebäck consistently identify the first natural frequency with strong repeatability across ROIs and yield modal stabilization patterns that agree well with OMA-based estimates. Horn–Schunck provides acceptable identification within the expected frequency band; however, its global smoothness constraint tends to attenuate true motion content and may introduce frequency shifts under low-amplitude responses. In contrast, the phase-based approach does not recover reliable modal parameters in the investigated configuration, exhibiting dominant components around 50 Hz rather than the structural mode near 26 Hz, suggesting susceptibility to experimental noise sources and insufficient motion content. Overall, the findings provide practical guidance for selecting optical-flow-based algorithms for vision-based structural identification and support their use as complementary tools in structural health monitoring applications.

1. Introduction

Structural Health Monitoring (SHM) aims to identify potential damage or performance degradation at an early stage by continuously or periodically monitoring and analyzing structural responses using sensors or measurement systems [1]. Early damage detection is essential for ensuring structural safety and reducing large-scale repair and maintenance costs [2]. Conventional SHM practice relies predominantly on contact-based sensors, such as accelerometers, displacement transducers, and strain gauges, which enable accurate estimation of modal parameters (natural frequencies, mode shapes, and damping ratios) and have therefore been widely used in both laboratory and field applications [3–5]. However, dense instrumentation typically requires substantial installation effort, cabling, and long-term maintenance, and measurements may be affected by sensor malfunctions and environmental variability (e.g., temperature/humidity), leading to drift and performance degradation [3]. Although alternative non-contact technologies such as fiber optic sensing and interferometric radar have been proposed, their high equipment cost, field deployment complexity, and operational constraints still limit widespread adoption in routine SHM [6–8].

With recent advances in imaging hardware and computational capacity, computer vision–based SHM has emerged as a flexible and comparatively low-cost alternative that can measure small displacements and vibration responses in a contactless manner [9,10]. Among vision-based techniques, Digital Image Correlation (DIC) tracks surface patterns between frames and can achieve high displacement resolution [11]. Optical flow methods estimate motion by analyzing intensity variations between consecutive frames and provide displacement–time histories at selected points or regions, often with favorable computational efficiency for real-time or near real-time processing [12]. Phase-based approaches infer motion from phase variations in the Fourier domain and have been reported to be effective for small-amplitude vibrations under suitable imaging conditions [13,14]. Deep learning–based vibration estimation methods have also been explored; however, their dependence on large training datasets and relatively high computational demand can restrict their practicality for many SHM scenarios [15–17]. Consequently, for practical and scalable SHM workflows, optical-flow and phase-based approaches remain attractive due to their implementation simplicity and processing speed, particularly when displacement is small, and instrumentation is constrained.

A growing number of studies demonstrate the feasibility of camera-based displacement measurements for modal identification in laboratory and field conditions. For example, vision-based displacement estimates have shown close agreement with reference sensors (e.g., laser sensors, accelerometers) in controlled experiments and bridge monitoring [18,19], while phase-based motion estimation has been successfully used for low-amplitude vibration characterization in certain applications [20]. Recent SHM-oriented optical flow studies also highlight the practicality

*Corresponding Author: volkan@ktu.edu.tr
Received 27 Jan 2026; Revised 04 Feb 2026; Accepted 04 Feb 2026
https://doi.org/10.36937/cebel.2026.11112

of industrial cameras and established algorithms such as Lucas–Kanade for operational vibration measurements [10]. Despite these advances, two methodological gaps remain insufficiently addressed in the literature. First, systematic comparisons of multiple optical-flow/phase-based algorithms performed under strictly identical conditions (same specimen, same excitation regime, and crucially, the same video data) are still limited, making it difficult to derive objective, implementation-independent guidance for algorithm selection. Second, integrated and user-oriented benchmarking tools that standardize the full workflow—ROI definition, scale calibration, displacement extraction, and frequency/modal identification—are scarce, which hinders reproducibility and the transfer of these methods to non-expert SHM users.

This study addresses these gaps by conducting a controlled, identical-data comparison of four widely used approaches—Lucas–Kanade, Farnebäck, Horn–Schunck, and a phase-based method—using high-speed video recordings acquired from a laboratory-scale single-story reinforced concrete (RC) frame subjected to impact excitation [23]. The focus is placed on the low-amplitude vibration regime, where algorithmic noise sensitivity, regularization effects, marker/texture characteristics, and imaging artifacts can substantially influence displacement extraction and downstream modal estimates. Importantly, the phase-based approach is included not as a presumed superior solution, but as a candidate method whose performance is known to be highly configuration-dependent (e.g., illumination characteristics, camera noise/quantization, spatial frequency content, and motion magnitude). Therefore, any observed limitation is interpreted as conditional on the investigated experimental configuration rather than as a universal conclusion.

To ensure a fair and repeatable comparison, all methods are implemented within a single graphical user interface (GUI) that provides a unified processing chain from video input to displacement extraction and export, followed by frequency-domain analysis (FFT) and Operational Modal Analysis (OMA) using PyOMA_GUI. Within this framework, algorithm performance is assessed in terms of frequency identification consistency across ROIs, signal stability under low-amplitude response, computational efficiency, and modal consistency in OMA outputs. Because the primary objective is a relative, algorithm-to-algorithm benchmarking under identical video conditions, the study is framed as a comparative assessment rather than an absolute accuracy validation against an external ground-truth sensor.

The main contributions of this study are summarized as follows:

- A controlled and identical-video comparison of Lucas–Kanade, Farnebäck, Horn–Schunck, and phase-based motion estimation for vibration identification in an RC frame;
- A unified GUI-based benchmarking workflow that standardizes ROI selection, scale calibration, displacement extraction, and data export to reduce user-dependent variability;
- Multi-domain evaluation combining FFT-based frequency identification and OMA-based modal consistency checks (PyOMA_GUI);
- Algorithm-specific insights for low-amplitude vibrations, including the practical effects of local feature sensitivity, dense-flow smoothing, global regularization, and configuration-dependent limitations of phase-based estimation.

The remainder of the paper is organized as follows. Section 2 summarizes the theoretical background of the investigated methods. Section 3 describes the unified processing workflow and implementation details. Section 4 presents the experimental setup and data acquisition. Section 5 discusses the comparative results in the time domain, frequency domain, and OMA domain. Finally, Section 6 concludes the study and provides practical guidance and limitations for SHM-oriented use.

2. Theory

Optical flow is a computer vision technique used to estimate the direction and magnitude of motion in the image plane by analyzing pixel intensity variations between consecutive image frames. The motion is modeled as a two-dimensional vector field, referred to as the optical flow field, defined for each pixel. In this study, four optical flow algorithms that are widely used in image-based structural vibration identification and rely on different underlying assumptions—namely, Lucas–Kanade, Farnebäck, Horn–Schunck, and phase-based optical flow methods—are considered.

2.1. Lucas–Kanade optical flow algorithm

Lucas–Kanade optical flow algorithm is a differential approach based on the brightness constancy assumption, which states that pixel intensities remain unchanged between consecutive frames [24]:

$$I(x,t) = I(x+\delta x, t+\delta t) \tag{1}$$

where I denotes the image intensity, x represents the spatial coordinates, t is time, and δx and δt correspond to small spatial and temporal increments. By linearizing Eq. (1) using a Taylor series expansion, the optical flow constraint equation is obtained as

$$\nabla I(x,t) \cdot u + I_t(x,t) = 0 \tag{2}$$

where ∇I(x,t) denotes the spatial gradient of the image intensity in two directions, I_t (x,t) represents the partial derivative with respect to time, and u denotes the two-dimensional optical flow vector. The Lucas–Kanade method assumes that all pixels within a small neighborhood share the same motion vector and estimates the solution using a least-squares formulation:

$$E(u) = \sum [\nabla I(x,t) \cdot u + I_t(x,t)]^2 \tag{3}$$

To capture large-scale motions, the method is implemented in a multi-scale framework using image pyramids [25]. The inter-scale flow combination is performed as follows [30]:

$$g_i = (2v_i),\ i = L \tag{4}$$

$$g_i = (2v_i + g_{i-1}),\ i < L \tag{5}$$

where L denotes the coarsest scale level, i represents the current scale level at which the computation is performed, v_i is the optical flow vector computed at the current scale, and g_{i-1} represents the flow propagated from the previous scale.

2.2. Farnebäck optical flow algorithm

The Farnebäck method is a dense optical flow approach that computes a motion vector for each pixel [27]. In this method, the local image intensity is approximated by a second-order polynomial:

$$f(x) \approx x^T A x + b^T x + c \tag{6}$$

where A is a symmetric coefficient matrix, b represents the linear coefficients, and c is a scalar term. Under the brightness constancy assumption, the spatial displacement between two consecutive frames is expressed as

$$f_2(x) = f_1(x - d) \tag{7}$$

where d represents the inter-pixel displacement. Accordingly, the displacement vector can be estimated solely from the difference between the linear coefficients:

$$u = -\frac{1}{2}(b_2 - b_1) \tag{8}$$

where u denotes the motion vector, while b_2 and b_1 represent the polynomial coefficients of the second and first frames, respectively. To reduce noise effects, the solution is computed over a neighborhood region. The relationship between the average curvature matrix and the gradient difference is given by

$$A(x)d(x) = \Delta b(x) \tag{9}$$

In this equation, the matrix $A(x)$ represents the average of the A matrices of the two consecutive frames, while $\Delta b(x)$ denotes the measure of the local gradient change between the frames. The final displacement estimate is obtained using a weighted least-squares formulation:

$$u(x) = \sum(wA^T A)^{-1} \cdot \sum(wA^T \Delta b) \tag{10}$$

where $w(\Delta x)$ denotes the weighting function.

2.3. Horn–Schunck optical flow algorithm

Horn–Schunck method minimizes a global energy function that enforces both brightness constancy and spatial smoothness of the flow field [28]:

$$E(u, v) = \iint \left[(I_x u + I_y v + I_t)^2 + \alpha^2(\|\nabla u\|^2 + \|\nabla v\|^2)\right] dx\, dy \tag{11}$$

In this equation, I_x, I_y, I_t denote the spatial image intensity derivatives in the $x-$ and $y-$ directions and the temporal derivative, respectively; u and v represent the horizontal and vertical components of the optical flow, and α is the smoothness parameter. The iterative update equations derived from the Euler–Lagrange formulation are expressed as

$$u^{(n+1)} = \bar{u}^{(n)} - \frac{I_x\left(I_x \bar{u}^{(n)} + I_y \bar{v}^{(n)} + I_t\right)}{\alpha^2 + I_x{}^2 + I_y{}^2} \tag{12}$$

$$v^{(n+1)} = \bar{v}^{(n)} - \frac{I_y(I_x \bar{u}^{(n)} + I_y \bar{v}^{(n)} + I_t)}{\alpha^2 + I_x{}^2 + I_y{}^2} \tag{13}$$

where the terms $\bar{u}$ and $\bar{v}$ represent the local averages computed from the previous iteration using a convolution kernel.

2.4. Phase-based optical flow algorithm

The phase-based method relies on the Fourier shift theorem, which states that a spatial translation between two images manifests as a linear phase difference in the frequency domain [31]. The phase correlation between two image windows is computed as

$$F = \mathcal{F}\{f\}, \quad G = \mathcal{F}\{g\}, \quad R = \frac{F\bar{G}}{|F\bar{G}|}, \quad r = \mathcal{F}^{-1}\{R\} \tag{14}$$

where f represents the image window extracted from the first frame, while g denotes the image window taken from the second frame, which is used to determine the relative spatial displacement between the two frames, and r represents the phase correlation surface obtained from the inverse Fourier transform of the normalized cross-power spectrum.

3. Method

The developed application was implemented using the Python programming language and is primarily based on the OpenCV, NumPy, SciPy, Pillow (PIL), Matplotlib, and Tkinter libraries. The software provides an integrated and reproducible workflow for extracting structural vibration characteristics from video recordings using multiple optical flow algorithms. All processing steps, from video input to frequency identification, are executed within a single Python-based GUI, ensuring that each method is evaluated under identical experimental conditions. This integrated design enables a fair and systematic comparison of the Lucas–Kanade, Farnebäck, Horn–Schunck, and phase-based optical flow approaches without introducing user-dependent inconsistencies.

Figure 1 illustrates the workflow of the developed application. The process begins with selecting and loading a video recording acquired during controlled vibration experiments. Subsequently, an ROI corresponding to the structural component under investigation is defined in order to confine the analysis to relevant image areas and reduce unnecessary computational cost. To convert pixel-based motion into physically meaningful quantities, a scale calibration step is performed using a known reference length in the image, allowing all displacement measurements to be expressed in real physical units.

Following ROI definition and scale calibration, optical flow–based displacement extraction is carried out within the selected regions. For each frame sequence, the chosen optical flow algorithm is consistently applied to all ROIs to obtain displacement–time histories. Frequency-domain analysis is subsequently performed on the resulting displacement signals using the fast Fourier transform (FFT) to identify dominant vibration frequencies. This step enables direct comparison of frequency identification accuracy among different optical flow methods. Finally, the displacement time histories and corresponding frequency information are exported in standard data formats (e.g., TXT or CSV). In this study, the exported data are transferred to the PyOMA_GUI application for operational modal analysis, where the identification of natural frequencies, damping ratios, and mode shapes is performed following the internal analysis workflow of the software. The processing steps of the PyOMA_GUI application are summarized in Figure 2.

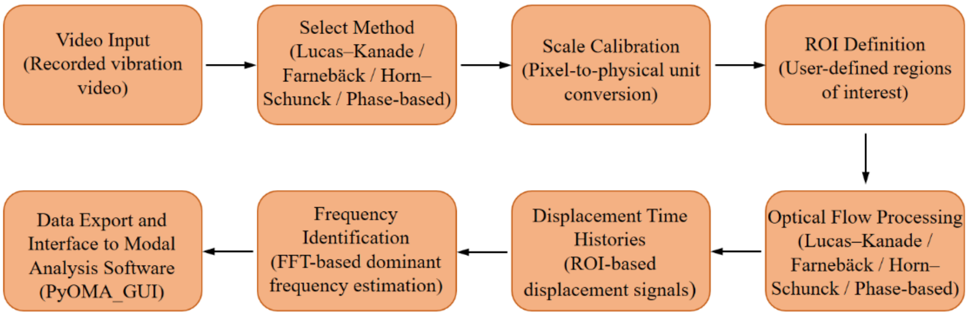

Figure 1. Workflow of the proposed vision-based vibration identification and modal analysis framework

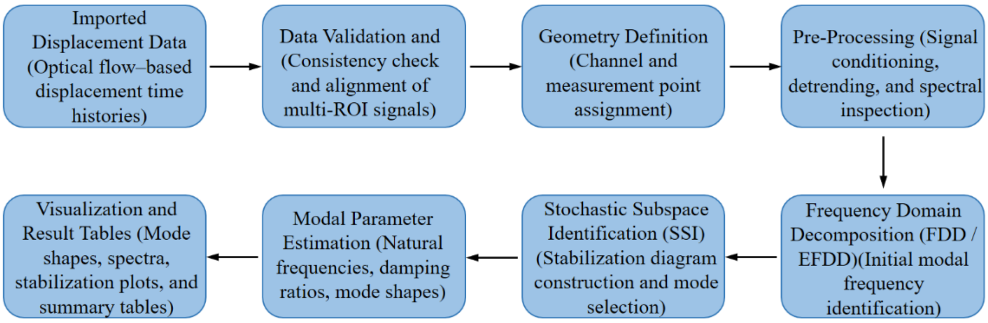

Figure 2. Workflow of the PyOMA_GUI software

By integrating video processing, ROI selection, scale calibration, displacement extraction, and frequency identification within a single workflow, the proposed system ensures consistency, repeatability, and transparency in the comparative evaluation of optical flow algorithms. This structure allows algorithmic differences to be assessed directly, independent of variations in user interaction or experimental setup, providing a suitable basis for performance-based comparisons in SHM applications.

4. Experimental Study

A portable and contactless high-speed video measurement system was employed for SHM and modal parameter identification. The imaging system consists of a CoaXPress-based VICTOREM industrial camera with a spatial resolution of 2064×1544 pixels, a frame rate of 216 FPS, and a pixel size of 3.45×3.45 μm², a DVR Express Core 2 CoaXPress recorder for high-volume image acquisition, and a computer for data processing [10, 32]. The system operates on mains power and can also be supplied by a portable generator for field applications. This configuration provides both high spatial resolution and high temporal sampling, enabling reliable measurement of sub-millimeter structural vibrations.

A single-story reinforced concrete (RC) frame was used as the experimental model. The total height of the frame is 1850 mm, consisting of a 400 mm foundation block, a 1250 mm column height, and a 200 mm beam depth. The total frame width is 1750 mm, with a clear span of 1250 mm. The column cross-sections were designed as 150×150 mm, while the beam cross-section was 150×200 mm. The foundation block has a thickness of 400 mm and a width of 600 mm. The geometric properties of the experimental model are illustrated in Figure 3.

The RC frame was rigidly fixed to the laboratory reaction wall using steel anchorage elements to provide a fixed-base boundary condition. The anchorage system ensured that the boundary conditions remained unchanged throughout the experiments. The imaging system was installed on a horizontal support positioned opposite the model. Since monitoring the entire frame with a single camera would reduce marker resolution and limit achievable frame rates, two cameras were employed. The cameras were aligned along the same viewing direction, with one focused on the QR code attached to the upper left beam–column joint and the other on the QR code at the upper right joint. The camera–specimen distance was optimized to minimize perspective distortion, while stable laboratory lighting conditions contributed to consistent image quality during the recordings. An overview of the experimental setup is shown in Figure 4. During the experimental measurements, video recordings with a duration of 120 s were acquired by adjusting the camera resolution and field of view. The RC frame was excited using an impact hammer to induce free-vibration responses, which were subsequently captured and analyzed using the recorded video data.

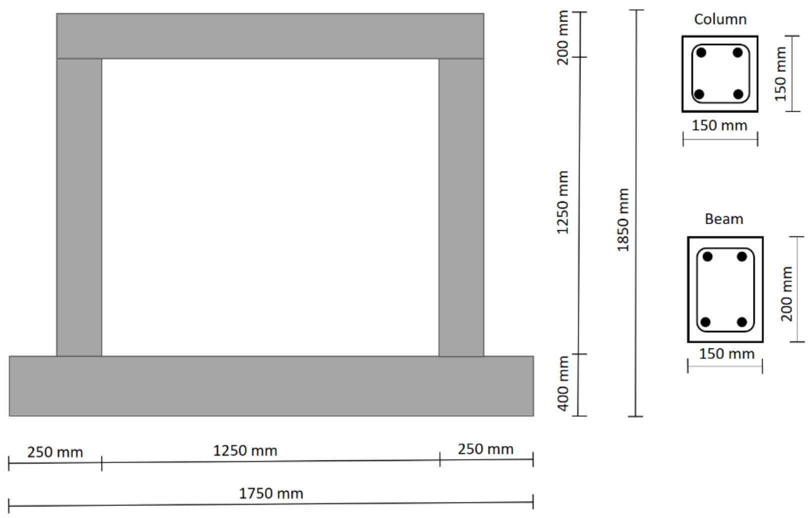

Figure 3. Dimensions of a single-story reinforced concrete frame model

To ensure consistency in the comparative evaluation of optical flow methods, the QR code at the upper left beam–column joint was defined as ROI-1, and the QR code at the upper right joint as ROI-2 (Figure 4). Since the ROIs were extracted from independent video recordings obtained by two different cameras, displacement–time histories and FFT results for ROI-1 and ROI-2 are presented separately. In contrast, for PyOMA_GUI-based modal analysis, displacement data from both ROIs were combined into a single dataset, allowing joint estimation of modal parameters.

Figure 4. ROI selection and video camera–based measurement setup for the single-story RC frame

Due to the negligible amplitude of vertical ($y-$ direction) vibrations, all analyses were performed using displacement data in the horizontal ($x-$ direction), which represents the dominant vibration behavior of the structure. Furthermore, considering the limitations imposed by the video frame rate, reliable frequency identification was achievable only for the first vibration mode. Accordingly, all frequency and modal analysis results presented in this study correspond to the first mode of the RC frame.

5. Results and Discussion

In this section, the results obtained from video recordings of the single-story RC frame using four different optical flow algorithms—Lucas–Kanade, Farnebäck, Horn–Schunck, and Phase-based—are comparatively presented and discussed. The evaluation is carried out based on displacement–time responses in the time domain, frequency-domain FFT results, and operational modal analysis (OMA) outputs obtained using the PyOMA_GUI environment. This integrated assessment enables a comprehensive investigation of each method in terms of sensitivity, stability, and modal parameter identification performance under low-amplitude vibration conditions. The total processing times were 696 s for the Lucas–Kanade method, 909 s for the Farnebäck method, 1671 s for the Horn–Schunck method, and 722 s for the phase-based method.

This study comparatively examines the consistency of Lucas–Kanade, Farnebäck, Horn–Schunck, and phase-based optical flow algorithms with each other, as well as their agreement with operational modal analysis (OMA) outputs obtained using PyOMA_GUI. The methods considered were previously evaluated based on their agreement with experimental (accelerometer-based) and numerical (finite element) references in studies conducted on a single-story steel frame model; it was reported that the differences in natural frequencies remained at approximately 0.6% when compared with accelerometer measurements [10, 23]. For this reason, no additional accelerometer measurements or ANSYS-based numerical validation were performed in the present study; instead, the relative performances of the methods were evaluated by directly comparing the differences with the PyOMA_GUI results.

The displacement–time histories obtained using the four optical flow algorithms are presented in Figures 5–12. These plots illustrate the horizontal displacement responses of the selected ROI points during the free-vibration phase following hammer excitation. Time-domain signals provide direct insight into the dynamic response of the structure and constitute the fundamental input for subsequent frequency-domain and modal analyses.

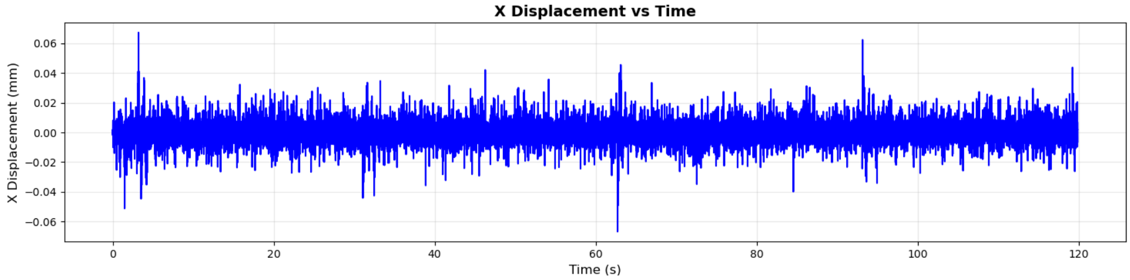

Figure 5. Displacement–time history obtained using the Lucas–Kanade method for ROI-1

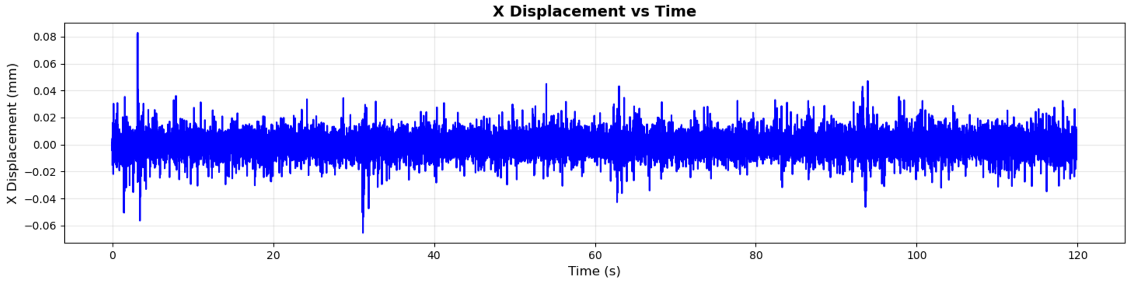

Figure 6. Displacement–time history obtained using the Lucas–Kanade method for ROI-2

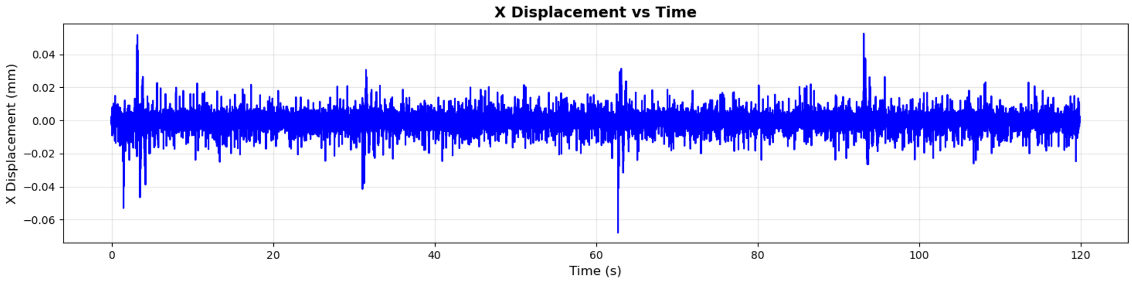

Figure 7. Displacement–time history obtained using the Farnebäck method for ROI-1

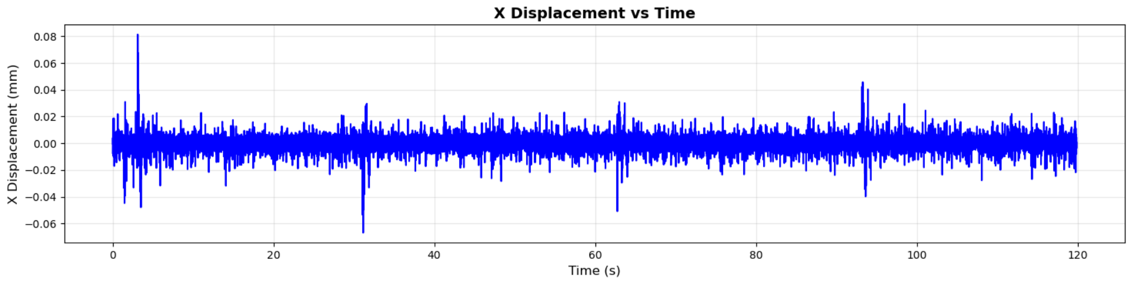

Figure 8. Displacement–time history obtained using the Farnebäck method for ROI-2

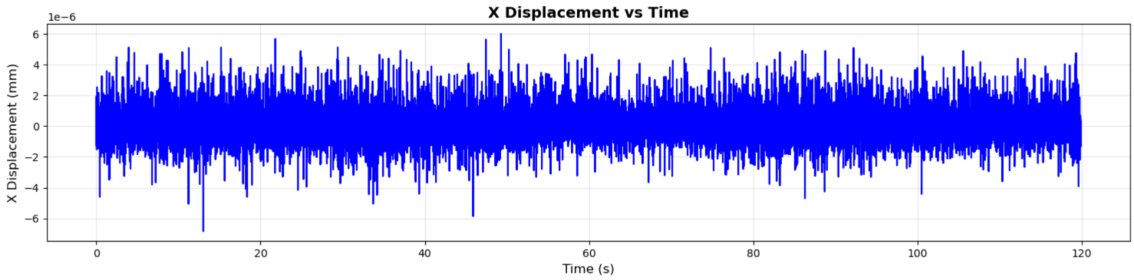

Figure 9. Displacement–time history obtained using the Horn–Schunck method for ROI-1

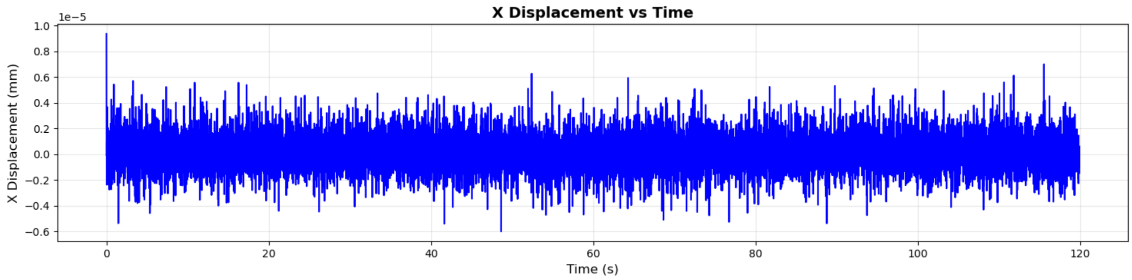

Figure 10. Displacement–time history obtained using the Horn–Schunck method for ROI-2

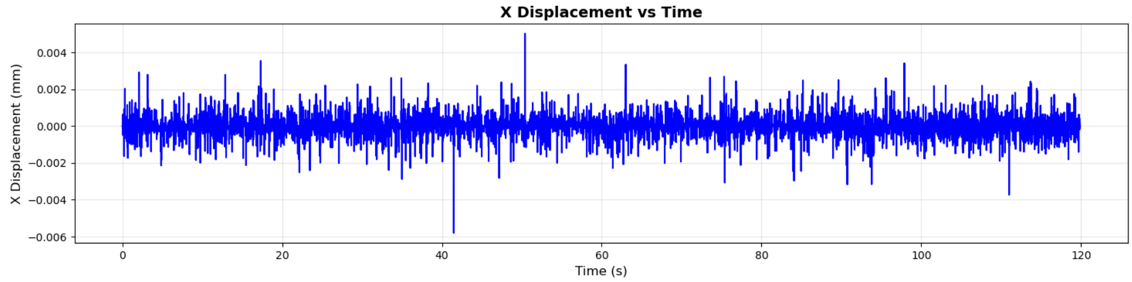

Figure 11. Displacement–time history obtained using the phase-based method for ROI-1

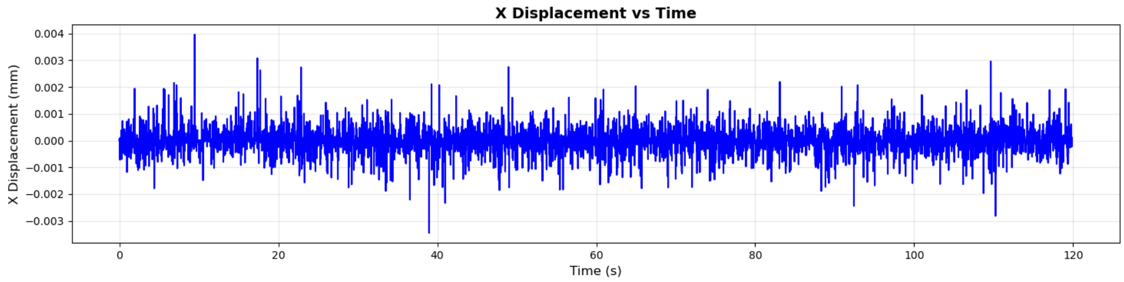

Figure 12. Displacement–time history obtained using the phase-based method for ROI-2

A joint evaluation of the signals obtained from ROI-1 and ROI-2 indicates that all four methods capture the general trend of the dominant vibration behavior of the structure. However, noticeable differences arise among the methods in terms of signal amplitude, noise sensitivity, and smoothness, particularly under the low-amplitude vibration conditions considered in this study.

The displacement–time responses derived using the Lucas–Kanade method exhibit relatively high amplitudes accompanied by irregular fluctuations for both ROIs. Due to its reliance on the local brightness constancy assumption and small analysis windows, even minor texture or illumination variations within the QR-code regions are interpreted as motion. This behavior increases the sensitivity of the method to noise, especially for low-amplitude vibrations. Nevertheless, the overall envelope of the signal preserves the primary vibration component, indicating that the essential characteristics of the free-vibration response are still represented.

The Farnebäck method yields the most balanced and smooth displacement–time signals among the four approaches. Its polynomial-based dense optical flow formulation effectively suppresses random brightness variations, resulting in more regular vibration signals. Although the displacement amplitudes for ROI-1 and ROI-2 are lower than those obtained with the Lucas–Kanade method, the reduced noise content demonstrates that Farnebäck provides a more stable representation of low-amplitude structural vibrations.

In contrast, the Horn–Schunck method exhibits a distinctly different behavior in the time domain. Owing to its global smoothness constraint, the displacement field is excessively regularized, leading to significant suppression of actual motion components. Consequently, the resulting signals for both ROIs display very low amplitudes and largely remain at the noise level. This outcome indicates that the ability of the Horn–Schunck method to distinguish true motion is limited under low-amplitude vibration conditions.

The phase-based method produces displacement–time signals with lower amplitudes than those of the Lucas–Kanade method, while maintaining a generally regular envelope. Due to its sensitivity to phase variations, limited high-frequency components appear at the initial stages of the signal. Although the overall trend is consistent with other methods, the low signal amplitude results in a reduced signal-to-noise ratio.

FFT results obtained for each optical flow method are presented in Figures 13–20. These spectra reveal the frequency components of the displacement signals and enable identification of the dominant vibration frequencies. FFT results derived from the Lucas–Kanade and Farnebäck methods show clear and consistent peaks within the same frequency band for both ROIs, demonstrating that, despite differences in time-domain noise characteristics, both methods reliably identify the natural frequency in the frequency domain. In particular, the irregular fluctuations observed in the time-domain Lucas–Kanade signals converge into a stable dominant peak in the frequency domain. The Farnebäck method yields FFT spectra characterized by lower amplitudes but cleaner and more stable frequency distributions. The limited noise level and orderly spectral structure indicate high reliability in natural frequency identification, with dominant peaks consistently appearing in the same frequency band as those obtained using the Lucas–Kanade method.

FFT outputs obtained using the Horn–Schunck method are notably low in amplitude and exhibit inconsistencies between the ROIs. While the natural frequency is correctly identified for ROI-2, a peak in a different frequency band appears for ROI-1. This inconsistency suggests that the strong smoothing inherent in the Horn–Schunck formulation can suppress true frequency components under low-amplitude vibration conditions.

For the phase-based method, no distinct peak corresponding to the natural frequency is observed in the FFT spectrum. The extremely low displacement amplitudes and the sensitivity of phase magnification to noise prevent effective separation of true motion components. As a result, the phase-based method proves inadequate for accurate fundamental frequency identification in this experimental setup.

The displacement time histories obtained from optical flow analyses were subsequently imported into the PyOMA_GUI environment, where singular value spectra, stabilization diagrams, and mode shapes were computed within the framework of operational modal analysis. These analyses provide a statistical and modal consistency check of the time- and frequency-domain results.

Singular value spectra presented in Figures 21–24 illustrate how vibration energy is distributed along the frequency axis. For Lucas–Kanade and Farnebäck methods, a sharp and pronounced peak is observed around 26 Hz, in strong agreement with both the time-domain signals and FFT results. The clarity of this peak and the limited spectral noise confirm that both methods achieve sufficient signal-to-noise ratios to reliably separate the dominant vibration mode. Singular value spectrum obtained using the Horn–Schunck method exhibits a different character. The dominant peak appears around 25 Hz, which does not fully coincide with the frequency estimates obtained from Lucas–Kanade and Farnebäck methods. Although the peak magnitude is relatively high and the spectral distribution is homogeneous, the slight frequency shift indicates that the strong smoothing effect of the algorithm may partially distort the true frequency content under low-amplitude vibrations. In contrast, the singular value spectrum obtained using the phase-based method is markedly weaker than those of the other approaches. The dominant peak observed in the 26 Hz band for the remaining methods does not appear; instead, a low-amplitude peak emerges near 50 Hz. This behavior demonstrates that the phase-based method fails to correctly separate the dominant vibration mode of the structure and does not provide a statistically reliable frequency estimate due to its low signal-to-noise ratio under the examined conditions.

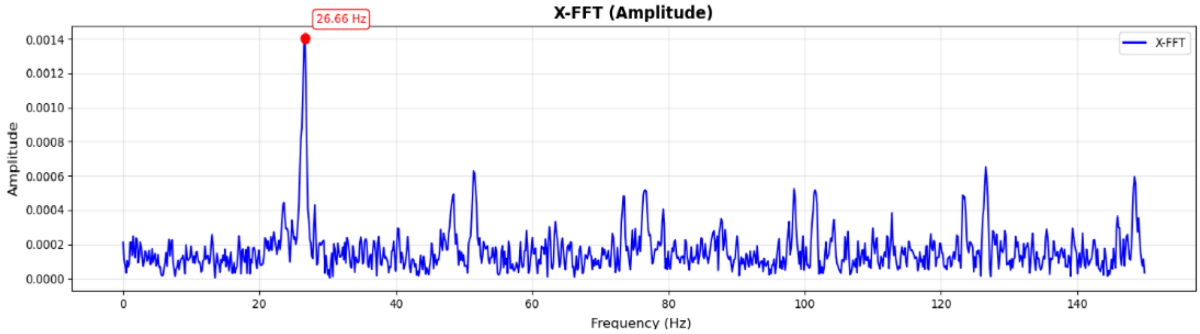

Figure 13. FFT spectrum obtained using the Lucas–Kanade method for ROI-1

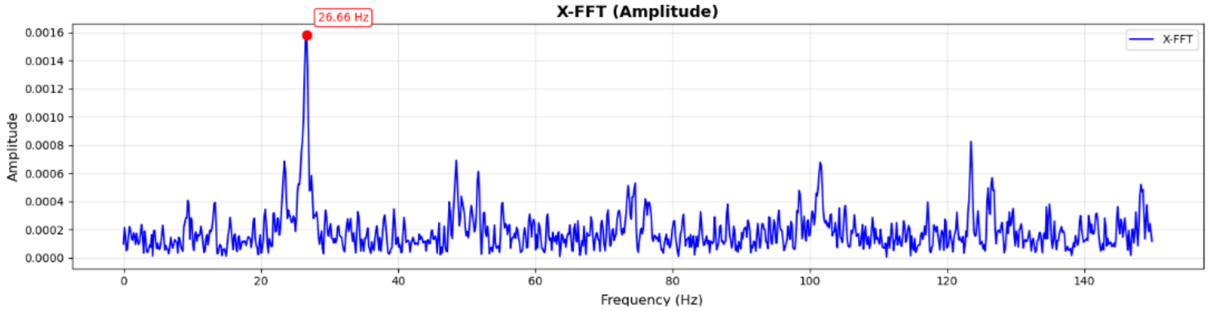

Figure 14. FFT spectrum obtained using the Lucas–Kanade method for ROI-2

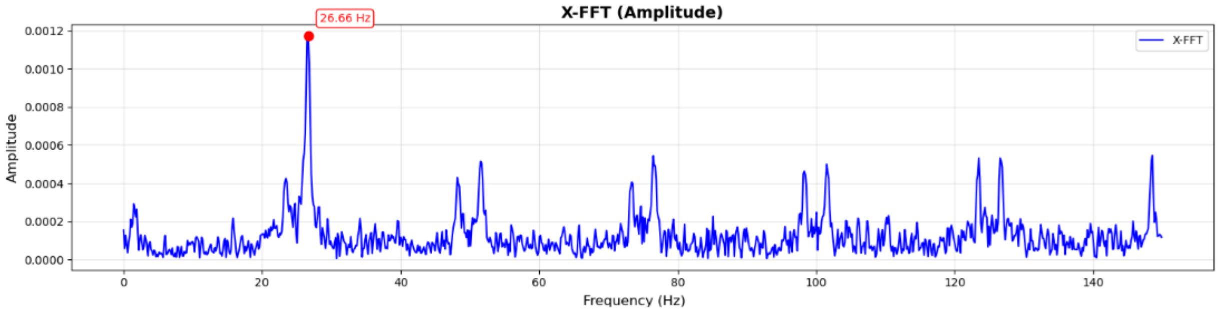

Figure 15. FFT spectrum obtained using the Farnebäck method for ROI-1

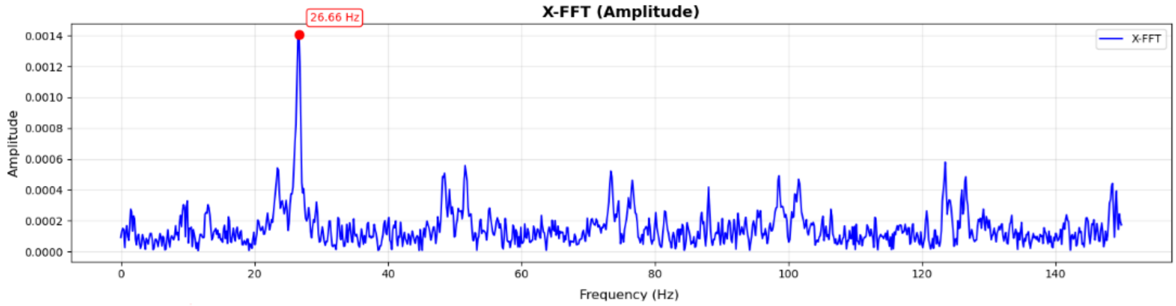

Figure 16. FFT spectrum obtained using the Farnebäck method for ROI-2

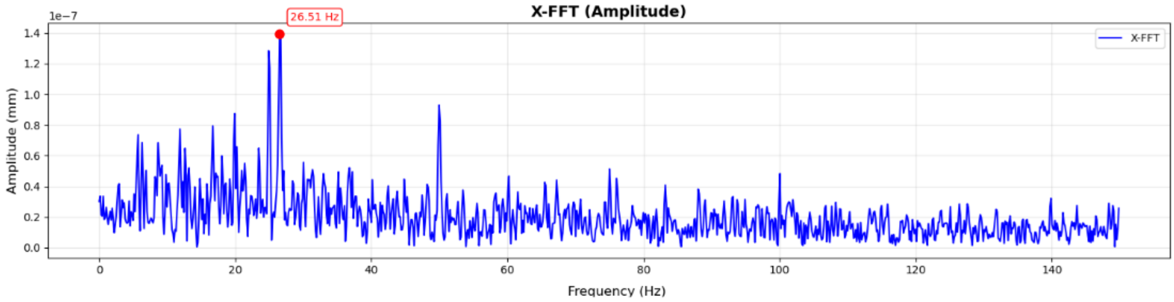

Figure 17. FFT spectrum obtained using the Horn–Schunck method for ROI-1

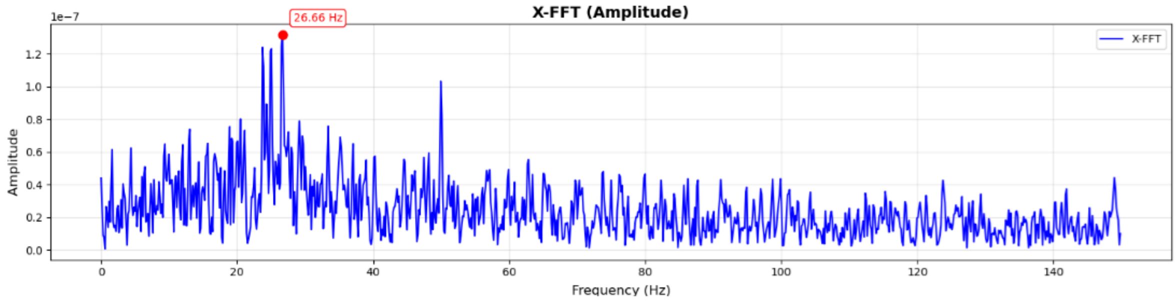

Figure 18. FFT spectrum obtained using the Horn–Schunck method for ROI-2

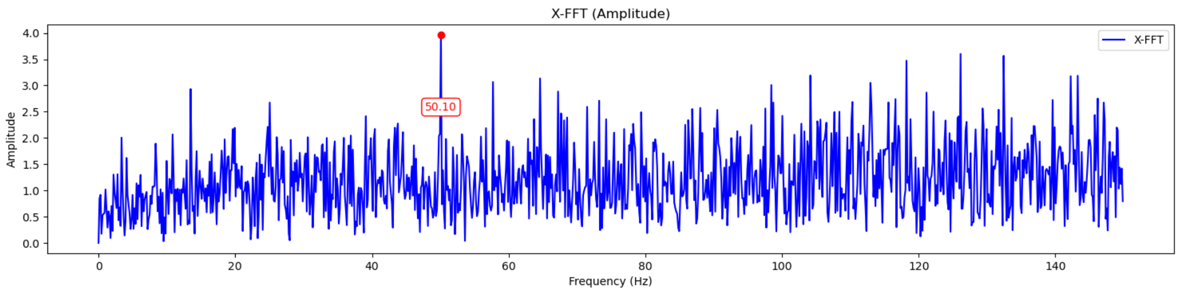

Figure 19. FFT spectrum obtained using the phase–based method for ROI-1

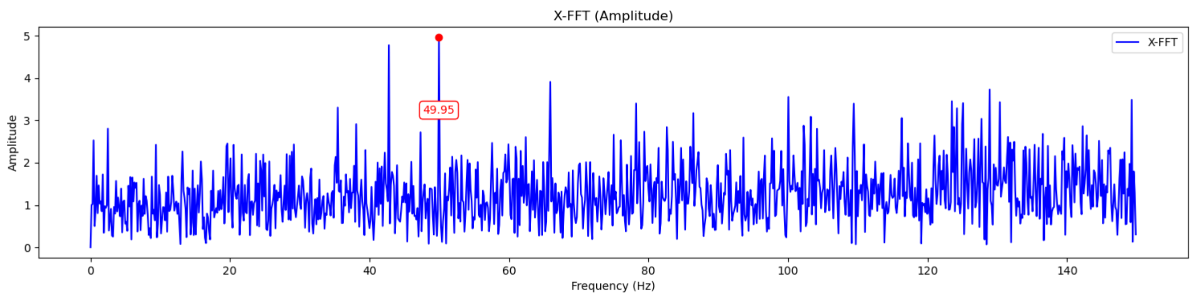

Figure 20. FFT spectrum obtained using the phase–based method for ROI-2

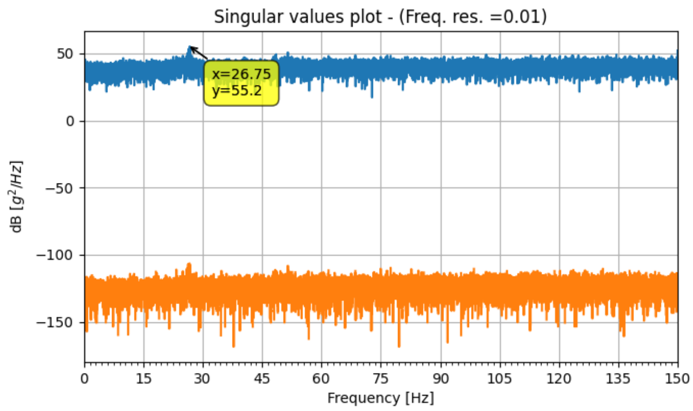

Figure 21. Singular values plot obtained using the Lucas–Kanade method

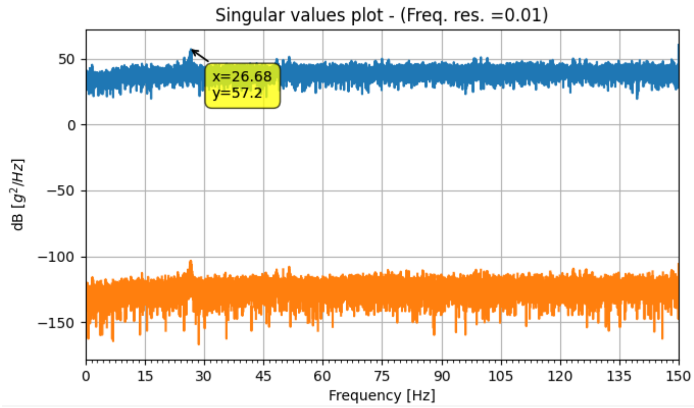

Figure 22. Singular values plot obtained using the Farnebäck method

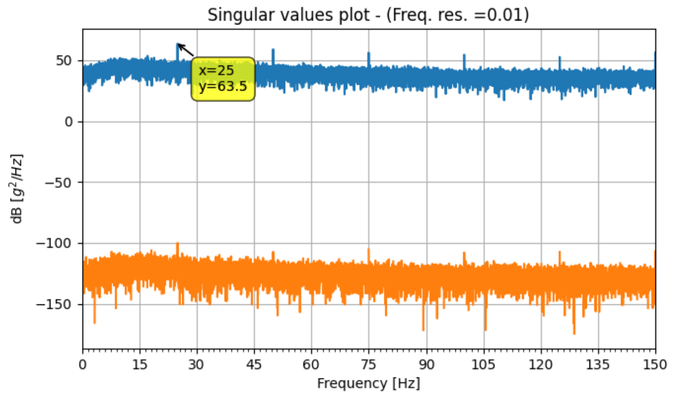

Figure 23. Singular values plot obtained using the Horn–Schunck method

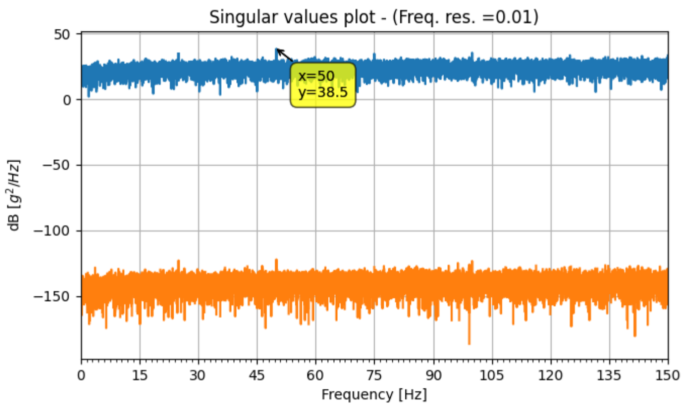

Figure 24. Singular values plot obtained using the phase–based method

Following the singular value analysis, stabilization diagrams were constructed using the SSI-cov and SSI-data approaches to assess modal stability (see Figures 25–28). Stabilization diagrams are employed to distinguish physical modes from numerical or noise-induced components by examining the consistency of system poles across increasing model orders. In the SSI-cov method, the system matrix is estimated based on the statistical properties of the input data, whereas the SSI-data approach directly models system dynamics from time-domain measurements. In both cases, vertically aligned and repeatedly appearing poles correspond to stable physical modes, while scattered poles indicate numerical or noise-related effects. The applied color coding (green: fully stable, yellow: partially stable, red: unstable) visually represents modal stability levels.

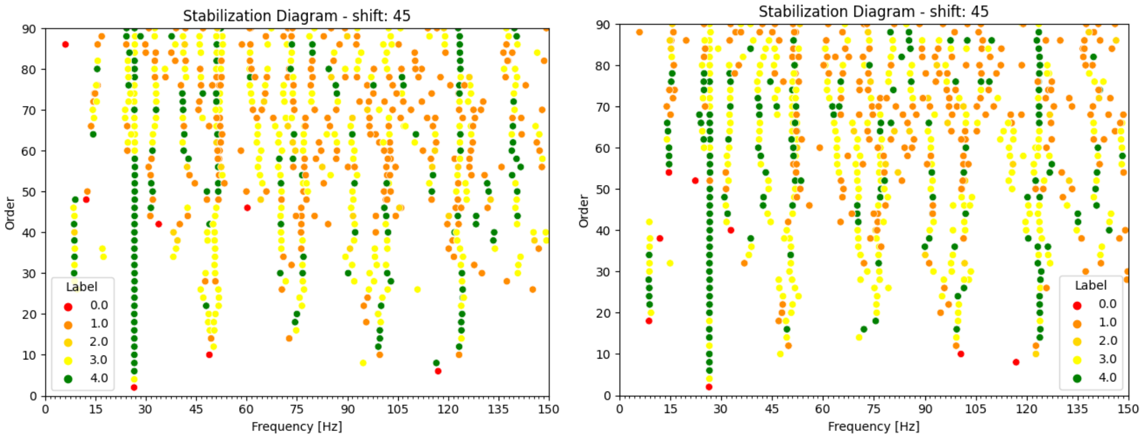

Figure 25. Stabilization diagram obtained using the Lucas–Kanade method with (a) SSI-cov and (b) SSI-data approaches

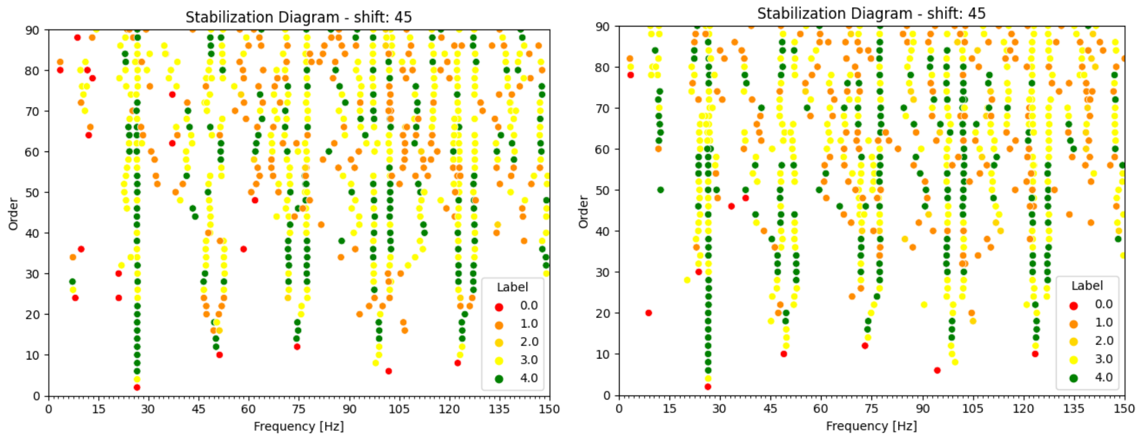

Figure 26. Stabilization diagram obtained using the Farnebäck method with (a) SSI-cov and (b) SSI-data approaches

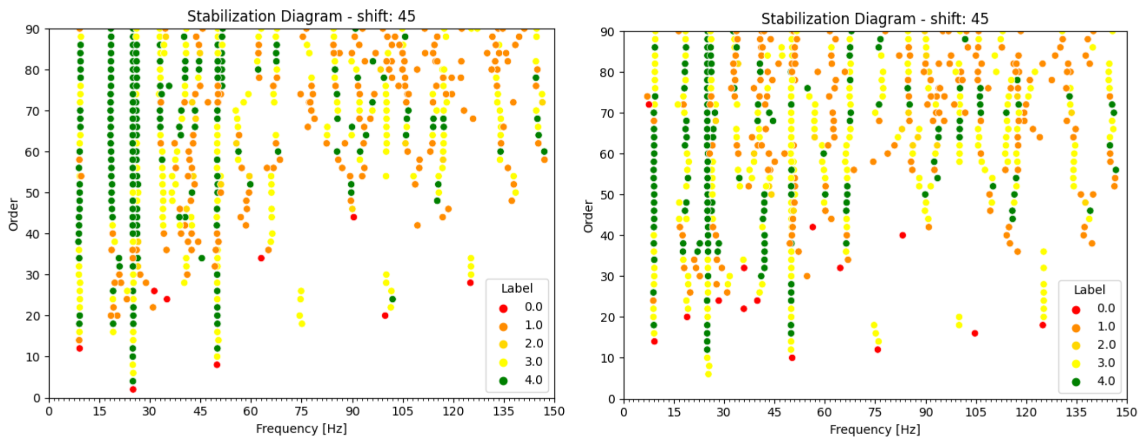

Figure 27. Stabilization diagram obtained using the Horn–Schunck method with (a) SSI-cov and (b) SSI-data approaches

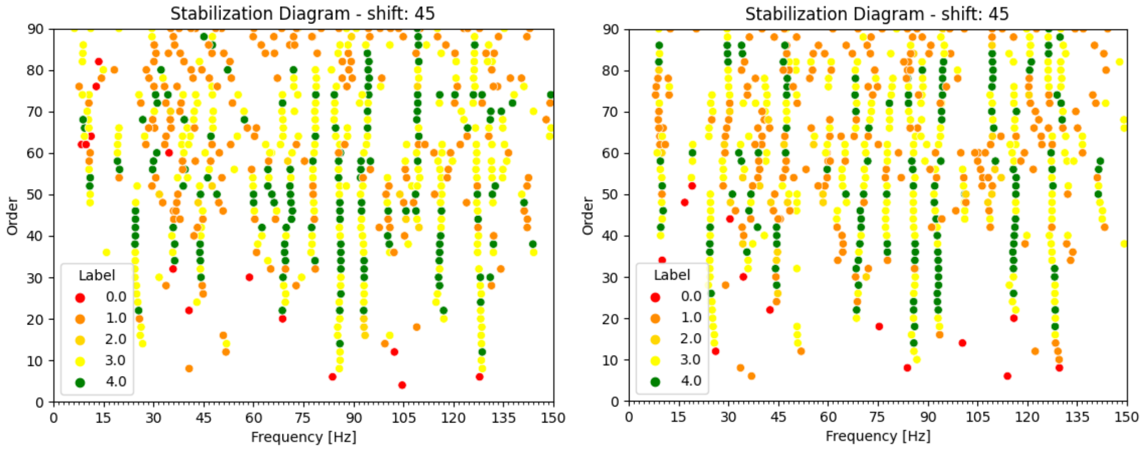

Figure 28. Stabilization diagram obtained using the phase–based method with (a) SSI-cov and (b) SSI-data approaches

For Lucas–Kanade, Farnebäck, and Horn–Schunck methods, the stabilization diagrams reveal well-defined and vertically aligned pole clusters around a 25–26 Hz band across increasing model orders. This pattern confirms that the first natural frequency is repeatedly and consistently identified as a stable physical mode. The density and continuity of stable poles are particularly pronounced for Lucas–Kanade and Farnebäck methods, highlighting their strong modal identification performance. Although the Horn–Schunck method also exhibits vertical alignment in the stabilization diagrams, fewer scattered poles appear in the higher frequency range compared to the other methods. This observation suggests that the global smoothing mechanism enhances resistance to numerical noise. However, minor deviations in the identified frequency indicate that accuracy may be limited under low-amplitude excitation. The stabilization diagrams obtained using the phase-based method differ substantially from those of the other approaches. No vertically aligned and repeatedly stabilized pole cluster appears near 26 Hz, and the poles remain dispersed across the frequency axis with inconsistent stability labels. This outcome confirms that the vibration data derived from the phase-based method does not provide sufficient quality for reliable modal identification.

Although the PyOMA_GUI environment allows mode shape extraction using FDD and EFDD techniques, the present study focuses on mode shapes obtained via the SSI-cov and SSI-data approaches. The resulting mode shapes (see Figures 29–32) indicate that the first bending mode is geometrically consistent for Lucas–Kanade, Farnebäck, and Horn–Schunck methods. In all three cases, negligible displacements at the base nodes and uniform horizontal translations at the upper nodes are observed, which are fully consistent with the expected first-mode deformation under fixed-base boundary conditions. The agreement between SSI-cov and SSI-data mode shapes further confirms the physical validity and stability of the identified modal parameters. Conversely, the mode shapes obtained using the phase-based method exhibit significant inconsistencies. Deviations in both magnitude and direction of upper-node displacements from the expected bending pattern indicate that this method does not yield reliable input data for modal analysis under the considered experimental conditions.

Overall, the results demonstrate that Lucas–Kanade and Farnebäck methods can reliably identify the natural frequency and provide consistent modal characteristics under low-amplitude vibration conditions. The Horn–Schunck method produces strong spectral responses in some cases but suffers from consistency limitations. The phase-based method, however, does not achieve satisfactory performance within the scope of this study.

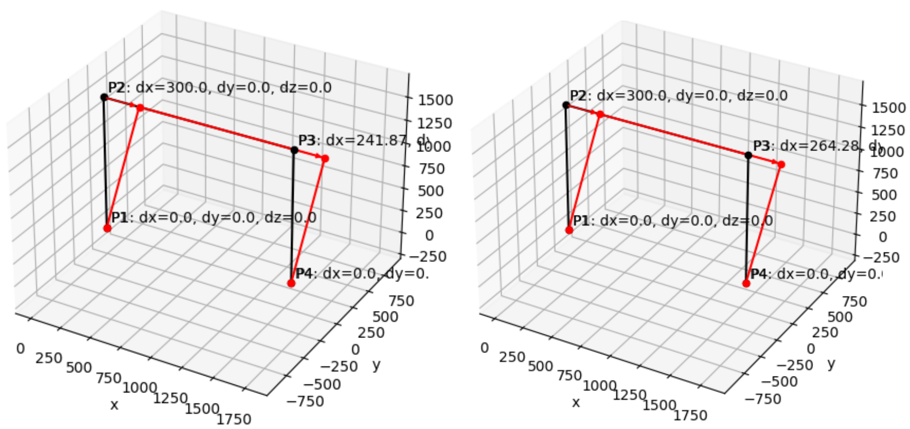

Figure 29. Mode shape obtained using the Lucas–Kanade method based on (a) SSI-cov and (b) SSI-data analyses

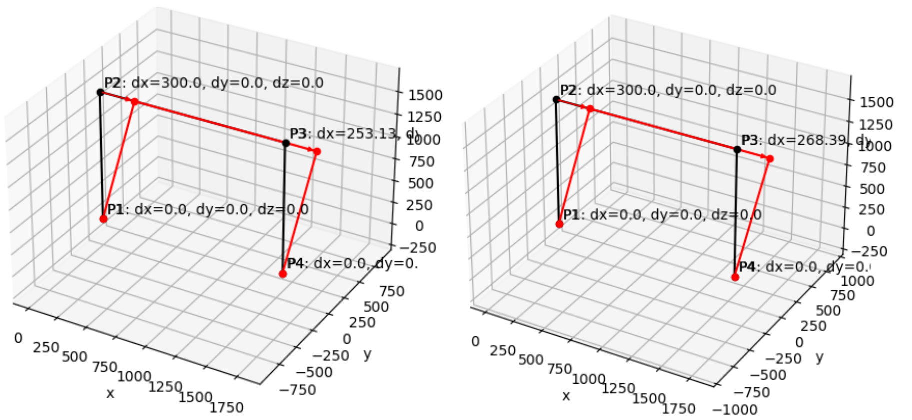

Figure 30. Mode shape obtained using the Farnebäck method based on (a) SSI-cov and (b) SSI-data analyses

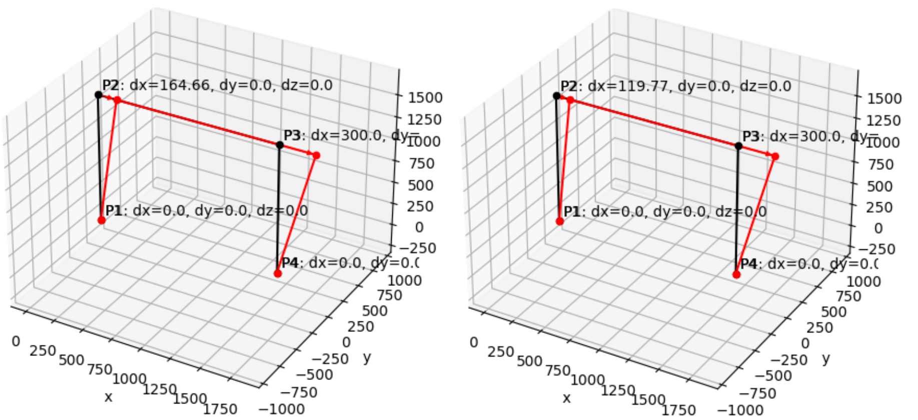

Figure 31. Mode shape obtained using the Horn–Schunck method based on (a) SSI-cov and (b) SSI-data analyses

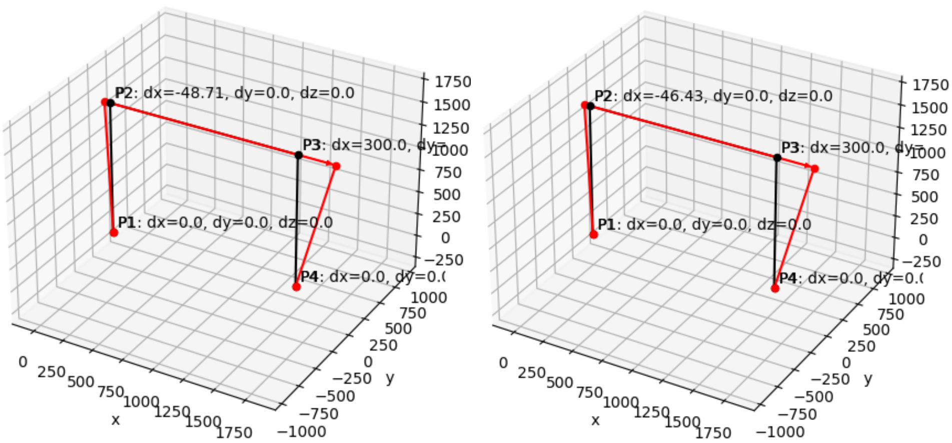

Figure 32. Mode shape obtained using the phase–based method based on (a) SSI-cov and (b) SSI-data analyses

Table 1. Comparison of results for the single-story RC frame

Method		Frequency (Hz)
Lucas-Kanade	ROI-1	26.66
	ROI-2	26.66
PyOMA_GUI	-	26.75
Farnebäck	ROI-1	26.66
	ROI-2	26.66
PyOMA_GUI	-	26.68
Horn-Schunck	ROI-1	26.51
	ROI-2	26.66
PyOMA_GUI	-	25.00
Phase-based	ROI-1	50.10
	ROI-2	49.95
PyOMA_GUI	-	50.00

Table 1 presents a direct comparison of the results obtained from different optical flow algorithms and the PyOMA_GUI-based modal analysis for identifying the first natural frequency of the single-story RC frame. While the optical flow methods were applied separately to the ROI-1 and ROI-2 regions extracted from two independent video recordings, the PyOMA_GUI analyses were performed using a single dataset obtained by combining the displacement responses from both ROIs.

Lucas–Kanade and Farnebäck methods yielded identical frequency values of 26.66 Hz for both ROI-1 and ROI-2. The consistency of the identified frequency across different spatial locations indicates the high repeatability and stable frequency detection capability of these two methods. Moreover, the corresponding frequencies obtained from the PyOMA_GUI analyses, calculated as 26.75 Hz and 26.68 Hz for Lucas–Kanade and Farnebäck methods, respectively, demonstrate strong agreement with the optical flow–based results.

For the Horn–Schunck method, the identified frequencies were 26.51 Hz for ROI-1 and 26.66 Hz for ROI-2. The slight discrepancy between the two ROIs suggests that, despite the global smoothing constraint inherent in the algorithm, the method remains moderately sensitive to local image characteristics. Nevertheless, the PyOMA_GUI result of 25.00 Hz indicates that the Horn–Schunck method is generally capable of capturing the first natural frequency within the correct range, albeit with a limited deviation when compared to the other methods.

In contrast, the phase-based method produced significantly higher frequency values of 50.10 Hz for ROI-1 and 49.95 Hz for ROI-2, which clearly deviate from the approximately 26.6 Hz frequency level identified by the other optical flow algorithms. This observation is further confirmed by the PyOMA_GUI result of 50.00 Hz, indicating that the phase-based method fails to correctly represent the dominant vibration mode of the experimental model. The observed failure should be interpreted as configuration-dependent (illumination, camera quantization, and motion magnitude) rather than as an intrinsic limitation of phase-based approaches.

Overall, the results demonstrate that Lucas–Kanade and Farnebäck methods can identify the first natural frequency with high accuracy and consistency in both optical flow–based and PyOMA_GUI-based analyses. The Horn–Schunck method exhibits acceptable performance with minor deviations, whereas the phase-based method does not provide reliable frequency estimates under the low-amplitude vibration conditions considered in this study.

6. Conclusions

In this study, user-friendly software was developed to enable the practical implementation and systematic comparison of vision-based vibration identification methods. Within this framework, four optical flow algorithms—Lucas–Kanade, Farnebäck, Horn–Schunck, and Phase-based—were experimentally evaluated using a single-story RC frame model. High-speed video recordings were processed to obtain displacement time histories, which were subsequently analyzed using both FFT-based frequency analysis and OMA through integration with PyOMA_GUI. This approach allowed the performance of the optical flow methods to be assessed comprehensively in terms of natural frequency identification, mode shape estimation, and modal stability.

The results indicate that Lucas–Kanade and Farnebäck algorithms are capable of identifying the first natural frequency with high accuracy and consistency under low-amplitude vibration conditions. The outcomes obtained in the time domain and frequency domain show strong agreement and a high level of consistency with the modal parameters extracted from PyOMA_GUI-based analyses. Moreover, the coincidence of frequency estimates derived from different ROI highlights the repeatability and stable performance of these two methods.

Horn–Schunck algorithm was generally able to capture the dominant vibration mode within the expected frequency range; however, partial deviations were observed under low-amplitude vibration conditions due to the global smoothness constraint inherent in the algorithm. The suppression of true displacement components in the time domain limited its frequency accuracy in certain cases. Nevertheless, the presence of stable pole clusters in the stabilization diagrams suggests that the Horn–Schunck method can provide acceptable modal identification performance under specific conditions.

In contrast, the phase-based optical flow method exhibited a markedly different behavior compared to the other approaches. For the RC frame characterized by low-amplitude vibrations, this method was unable to sufficiently separate true vibration components from noise and consistently overestimated the natural frequency. The combined evaluation of FFT results, singular value spectra, stabilization diagrams, and mode shapes clearly demonstrates that the phase-based method failed to produce reliable modal parameters under the experimental conditions considered in this study.

The operational modal analyses performed by transferring the optical-flow-derived displacement data into the PyOMA_GUI environment further supported the findings obtained in the time and frequency domains. In particular, the displacement signals extracted using Lucas–Kanade and Farnebäck algorithms resulted in physically meaningful and stable modal parameters. The stabilization diagrams and mode shapes obtained from the SSI-cov and the SSI-data approaches confirmed that these two methods accurately represented the first bending mode with correct geometric characteristics.

Overall, this study demonstrates that computer vision–based optical flow techniques can be effectively employed in SHM applications. Among the evaluated methods, Lucas–Kanade and Farnebäck algorithms provide reliable and practical solutions for natural frequency and mode shape identification under low-amplitude vibration conditions. While the Horn–Schunck method exhibits acceptable performance in limited cases, caution is required when applying the phase-based method under similar experimental conditions. The comparative framework and findings presented in this study are expected to contribute to more informed selection and application of vision-based modal analysis techniques in engineering practice.

Acknowledgements

The authors would like to thank Dr. Fezayil Sunca and Tunahan Aslan for their contributions and support during the experimental studies.

Declaration of Conflict of Interests

The authors declare that there is no conflict of interest. They have no known competing financial interests or personal relationships that could have appeared to influence the work reported in this paper.

References

[1.] Farrar, C.R., Worden, K., Structural health monitoring: A machine learning perspective. John Wiley & Sons, Chichester (2012).

[2.] Carden, E.P., Fanning, P., Vibration based condition monitoring: A review. Structural Health Monitoring 3(4) (2004) 355–377.

[3.] Doebling, S.W., Farrar, C.R., Prime, M.B., A summary review of vibration-based damage identification methods. The Shock and Vibration Digest 30(2) (1998) 91–105.

[4.] Amafabia, D.M., Montalvão, D., David-West, O., Haritos, G., A review of structural health monitoring techniques as applied to composite structures. Structural Durability & Health Monitoring 11 (2017) 91–147.

[5.] Kahya, V., Şimşek, S., Toğan, V., Vibration-based damage detection in anisotropic laminated composite beams by a shear-deformable finite element and harmony search optimization. Structural and Multidisciplinary Optimization 65 (2022) 181.

[6.] Li, S., Wu, Z., Development of distributed long-gage fiber optic sensing system for structural health monitoring. Structural Health Monitoring 6 (2007) 133–143.

[7.] Feng, M.Q., Kim, D.H., Novel fiber optic accelerometer system using geometric moiré fringe. Sensors and Actuators A: Physical 128 (2006) 37–42.

[8.] Gentile, C., Bernardini, G., An interferometric radar for non-contact measurement of deflections on civil engineering structures: Laboratory and full-scale tests. Structure and Infrastructure Engineering 6 (2010) 521–534.

[9.] Feng, D., Feng, M.Q., Identification of structural stiffness and excitation forces in time domain using noncontact vision-based displacement measurement. Journal of Sound and Vibration 406 (2017) 15–28.

[10.] Hacıefendioğlu, K., Kahya, V., Limongelli, M.G., Okur, F.Y., Altunışık, A.C., Aslan, T., Pembeoğlu, S., Duman, C., Bostan, A., Aleit, H., Applications of optical flow methods and computer vision in structural health monitoring for enhanced modal identification. Structures 69 (2024) 107414.

[11.] Wang, Z., Hien, V.H., Nguyen, H., Le, M.B., Digital image correlation in experimental mechanics and image registration in computer vision: Similarities, differences and complements. Optics and Lasers in Engineering 65 (2015) 18–27.

[12.] Xu, Y., Brownjohn, J.M.W., Review of machine-vision based methodologies for displacement measurement in civil structures. Journal of Civil Structural Health Monitoring 8(1) (2018) 91–110.

[13.] Fleet, D.J., Jepson, A.D., Computation of component image velocity from local phase information. International Journal of Computer Vision 5(1) (1990) 77–104.

[14.] Wadhwa, N., Rubinstein, M., Durand, F., Freeman, W.T., Phase-based video motion processing. ACM Transactions on Graphics 32(4) (2013) 80.

[15.] Toh, G., Park, J., Review of vibration based structural health monitoring using deep learning. Applied Sciences 10(5) (2020) 1680.

[16.] Pan, B., Qian, K., Xie, H., Asundi, A., Two-dimensional digital image correlation for in-plane displacement and strain measurement: A review. Measurement Science and Technology 20(6) (2009) 062001.

[17.] Chen, J.G., Wadhwa, N., Cha, Y.J., Durand, F., Freeman, W.T., Buyukozturk, O., Modal identification of simple structures with high-speed video using motion magnification. Journal of Sound and Vibration 345 (2015) 58–71.

[18.] Feng, D., Feng, M.Q., Ozer, E., Fukuda, Y., A vision-based sensor for noncontact structural displacement measurement. Sensors 15(7) (2015) 16557–16575.

[19.] Dong, C.Z., Ye, X.W., Jin, T., Identification of structural dynamic characteristics based on machine vision technology. Measurement 126 (2018) 405–416.

[20.] Sarrafi, A., Mao, Z., Niezrecki, C., Poozesh, P., Vibration-based damage detection in wind turbine blades using phase-based motion estimation and motion magnification. Journal of Sound and Vibration 421 (2018) 300–318.

[21.] Kromanis, R., Kripakaran, P., A multiple camera position approach for accurate displacement measurement using computer vision. Journal of Civil Structural Health Monitoring 11 (2021) 661–678.

[22.] Kalybek, M., Modal analysis and finite element model updating of civil engineering structures using camera-based vibration monitoring systems. PhD Thesis, University of Leicester, Leicester (2022).

[23.] Gençcelep, S., Titreşim verileri kullanılarak bilgisayarlı görü tabanlı yapı sağlığı izlemesinde optik akış algoritmalarının karşılaştırmalı analizi. MSc Thesis, Karadeniz Technical University, Graduate School of Natural Sciences, Trabzon (2025) (in Turkish).

[24.] Lucas, B.D., Kanade, T., An iterative image registration technique with an application to stereo vision. Proceedings of the 7th International Joint Conference on Artificial Intelligence (IJCAI'81), Vancouver, Canada (1981) 674–679.

[25.] Bouguet, J.Y., Pyramidal implementation of the affine Lucas-Kanade feature tracker: Description of the algorithm. Intel Corporation, Microprocessor Research Labs, California (2001).

[26.] Brox, T., Malik, J., Large displacement optical flow: Descriptor matching in variational motion estimation. IEEE Transactions on Pattern Analysis and Machine Intelligence 33(3) (2011) 500–513.

[27.] Farnebäck, G., Two-frame motion estimation based on polynomial expansion. Proceedings of the 13th Scandinavian Conference on Image Analysis, Springer (2003) 363–370.

[28.] Horn, B.K.P., Schunck, B.G., Determining optical flow. Artificial Intelligence 17(1–3) (1981) 185–203.

[29.] Pérez, J.S., Meinhardt, E., Kondermann, D., Horn–Schunck optical flow with a multi-scale strategy. Image Processing Online 3 (2013) 151–172.

[30.] Al-Qudah, S., Yang, M., Large displacement detection using improved Lucas-Kanade optical flow. Sensors 23 (2023) 3152.

[31.] Kuglin, C.D., Hines, D.C., The phase correlation image alignment method. IEEE International Conference on Cybernetics and Society, Proceedings (1975) 163–165.

[32.] Yıldırım, A., Yapıların modal parametrelerinin yüksek hızlı kamera tabanlı yer değiştirme ölçümleri ile elde edilmesi. MSc Thesis, Karadeniz Technical University, Graduate School of Natural Sciences, Trabzon (2024) (in Turkish).

How to Cite This Article

Gençcelep, S., Kahya, V., and Hacıefendioğlu, K., Comparative performance assessment of optical flow methods for vision-based structural identification using vibration data, Civil Engineering Beyond Limits, 2(2026), 11112.
https://doi.org/10.36937/cebel.2026.11112